

Rapid prototyping and parametric optimization of plastic acoustofluidic devices for blood–bacteria separation

R. Silva^{1,2,3}  · P. Dow³ · R. Dubay³ · C. Lissandrello³ · J. Holder³ · D. Densmore^{1,2} · J. Fiering³

© Springer Science+Business Media, LLC 2017

Abstract Acoustic manipulation has emerged as a versatile method for microfluidic separation and concentration of particles and cells. Most recent demonstrations of the technology use piezoelectric actuators to excite resonant modes in silicon or glass microchannels. Here, we focus on acoustic manipulation in disposable, plastic microchannels in order to enable a low-cost processing tool for point-of-care diagnostics. Unfortunately, the performance of resonant acoustofluidic devices in plastic is hampered by a lack of a predictive model. In this paper, we build and test a plastic blood–bacteria separation device informed by a design of experiments approach, parametric rapid prototyping, and screening by image-processing. We demonstrate that the new device geometry can separate bacteria from blood while operating at 275% greater flow rate as well as reduce the power requirement by 82%, while maintaining equivalent separation performance and resolution when compared to the previously published plastic acoustofluidic separation device.

Electronic supplementary material The online version of this article (doi:[10.1007/s10544-017-0210-3](https://doi.org/10.1007/s10544-017-0210-3)) contains supplementary material, which is available to authorized users.

✉ R. Silva
rjsilva@bu.edu
J. Fiering
jfiering@draper.com

¹ Boston University Department of Electrical and Computer Engineering, 8 Saint Mary's St., Boston, USA

² Biological Design Center, 610 Commonwealth Ave, Boston, USA

³ Draper, 555 Technology Square, Cambridge, MA 02139, USA

Keywords Microfluidics · Acoustics · Blood · Bacteria · Separation · Acoustophoresis

1 Introduction

Separation and concentration of particles and cells via microfluidic acoustic manipulation has emerged as a versatile method for rapid and efficient fluid sample processing. It is an attractive alternative over other fluid manipulation techniques because it is label-free, requires no electrodes or specialized structures in the microchannel, and has the potential for scale-up for high throughput processing (Antfolk and Laurell 2017; Bhagat et al. 2010). In so-called “bulk” acoustic microfluidic devices, the acoustophoretic force is maximized as the fluid-filled microchannel resonates as a cavity and establishes a standing pressure wave transverse to flow. Hence, the magnitude of the acoustic force on a particle depends strongly on the physical dimensions of the channel and walls, which must be appropriately selected for the ultrasonic excitation frequency (Bruus 2012).

The force exerted on a particle by the acoustically-driven standing pressure wave scales cubically with particle diameter (Settnes and Bruus 2012). Thus, acoustic manipulation is particularly well suited for isolating bacterial samples from larger blood components such as red blood cells (RBCs) and white blood cells (WBCs) based purely on relative differences in size (Ohlsson et al. 2016; Li et al. 2016). This is useful as downstream assays, such as antimicrobial susceptibility testing, benefit from a purified, well-defined input with reduced contamination of mammalian cell components.

Silicon, glass, or metal devices are commonly used for acoustophoresis because the rigid channel walls provide

a near ideal acoustic boundary against the sample fluid, enhancing the required standing wave resonance (Barnkob and Bruus 2009; Hill et al. 2008). This ideal boundary simplifies design because one-dimensional analysis can be used to estimate the resonant modes in the channel-fluid system. However, the rigid materials used in these devices are relatively expensive and slow to manufacture, have limited compatibility with many biological samples, and pose challenges to produce as disposable laboratory tools (Nge et al. 2013). On the other hand, our recent work has demonstrated acoustophoresis in plastic, showing that acoustic separation of RBCs is possible in polystyrene, opening the door to low-cost diagnostic and therapeutic devices (Mueller et al. 2013).

However, the design of optimized plastic acoustofluidic devices is hampered by complex boundary conditions relative to those of more rigid materials, and a satisfactory predictive model is not yet established, because the one-dimensional approximations are inaccurate and the channel walls can no longer be considered ideally rigid (Mueller et al. 2013). Moreover, even for rigid materials, a sophisticated 2-dimensional analysis does not appear to easily predict experimental performance in detail (Garofalo et al. 2016; Bora and Shusteff 2015). To further optimize the geometry of acoustic microfluidics in plastic, a parametrized experimental investigation provides an expanded database for comparison with simulation and can give performance improvements without the need for simulation.

This study used rapid prototyping, statistical design of experiments, and rapid experimental screening to obtain a

better-performing device geometry when compared to the only other plastic, acoustofluidic blood–bacteria separation device in literature (Mueller et al. 2013), which will be referred to as the *baseline*. The devices tested varied in cross section dimensions. The baseline was designed in accordance with the existing one-dimensional hard-wall theory and no further optimization had been attempted.

While plastic acoustofluidic devices can be produced in volume using methods such as hot embossing or injection molding (Heckele and Schomburg 2003), prototyping test geometries in small batches could become a costly endeavor. We minimized fabrication costs by manufacturing chips on-site through the use of an automated, rapid prototyping software framework in conjunction with a new class of inexpensive, desktop computer numerical controlled (CNC) micromills.

Devices were screened in rapid succession using an image-based performance parameter of RBC acoustophoresis, described in Section 3.2, while varying two measures of merit: dissipated power and volumetric flow rate. As a final validation, the improved design was compared to the baseline in the task of separating bacteria from blood and shown to achieve comparable separation with significant advantages in the figures of merit. This improved device offers increased throughput and reduced power requirements and could improve performance in future point-of-care plastic acoustofluidic devices.

Figure 1 illustrates the iterative workflow used in conducting the study, further described in Section 2. Section 2 summarizes the approach used to design variable chip

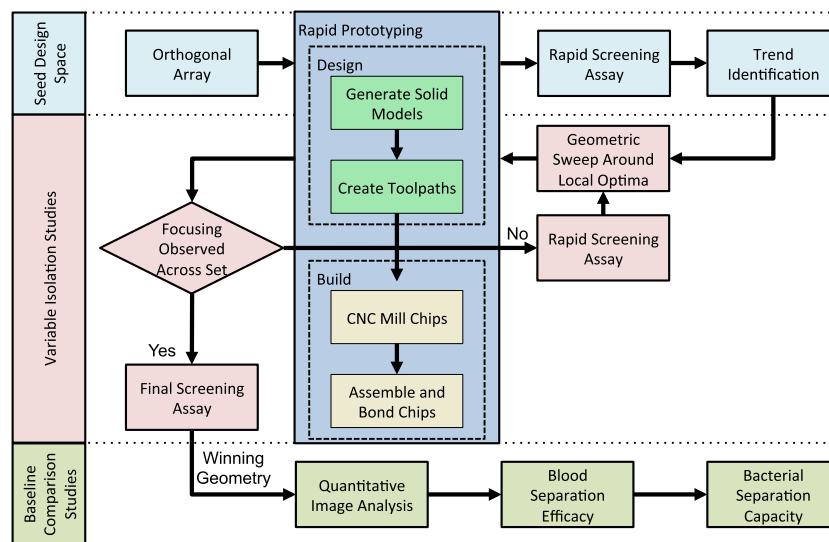


Fig. 1 Iterative rapid prototyping and testing workflow. The design space was first seeded using a design of experiments tool known as an orthogonal array, which minimizes the number of necessary experiments when compared to a full-factorial experimental analysis (Section 4.2). Trends were then identified within single geometric

variables and experimentally explored. These variable isolation studies were repeated until a fully functional design set was achieved (Section 4.3). The best performing device geometry emerging from the workflow, Chip 2.0, is then compared to the baseline (Section 4.4)

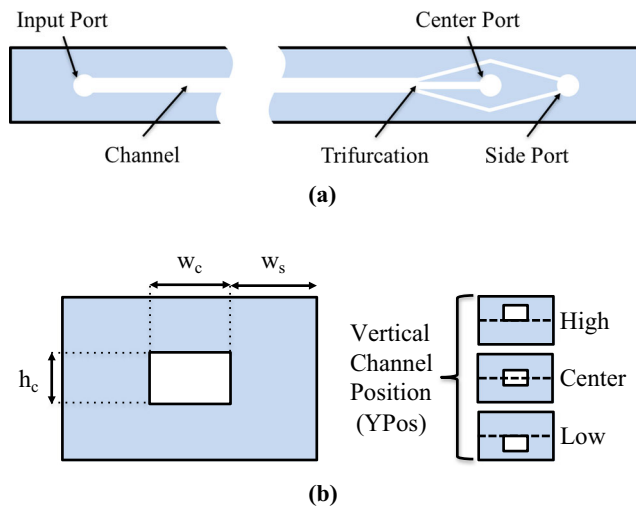


Fig. 2 Acoustic separation device. **a** Complete trifurcated microfluidic separation chip. **b** Definitions for each two-dimensional geometry included in the study. Note that the definitions apply to the fluidic channel upstream of the trifurcation

geometries and defines the two types of tests used in the screening phase of the workflow. Section 3 outlines the methods used to screen separation performance from microscope images. Finally, Section 4 presents the results of the device screening as well as the winning design's performance when compared to that of the baseline geometry.

Figure 2a is a top view illustration of the trifurcated acoustic separation device. The device functions by focusing large particles, such as RBCs and WBCs, to the center port, while smaller particles (ex., platelets, bacteria, etc.) are collected at the side port. This trifurcated device is used in the blood and bacterial separation experiments. In order to reduce manufacturing complexity, devices screened using the methods outlined in Sections 2.2.1 and 2.2.2 consist only of the input port; fluid channel, defined as the channel upstream of the trifurcation; and a single output port. The cross-sectional geometries, defined in Fig. 2b, apply to this simplified device design.

2 Experimental methodology

2.1 Rapid prototyping

This study relied upon the ability to design and fabricate iterations of chip geometries in a rapid process informed

```
chip (Wc=0.55 ,Hc=0.25 ,Ws=0.85 ,YPos=high );
```

Listing 1 The custom OpenSCAD library allows solid model creation using just a single line of code

```
include<chip.scad>

wc=[1.5,1,0.5];
ws=[0.5,1.5,2.5];
hc=[0.1,0.2,0.25];
ypos=[high,high,high];
Spacing=0.79375; //End Mill Diameter

numChips=len(wc); // Total chips to make

module chipLayout(){
  // Iterate over number of chips
  for (i=[0:(numChips-1)]){
    let (ChipY=wc[i]+ws[i]*2){
      // Correctly space chips apart
      translate([0,2*(ChipY+Spacing),0])
      chip(Wc=wc[i],Hc=hc[i],Ws=ws[i],YPos=
        ypos[i]);
    }
  }
}
```

Listing 2 The single line of code in Listing 1 can then be iterated upon to form an array of different device geometries that can be sent directly to a CAM tool for toolpath generation

by experimental tests. The traditional workflow of conventional machining requires a fully specified mechanical drawing and changes to the design may demand regeneration of the solid model and revised setup of the milling instrument. This section describes how these limitations were mitigated using free and open-source design software in conjunction with a \$3,199 USD desktop micromill (Othermill Pro, Other Machine Co., Berkeley, CA, USA). Microchannels with parameterized dimensions were systematically fabricated with a minimum of operator intervention.

2.1.1 Design generation

Three levels of software are required to design and fabricate a novel chip geometry using a computer numerical control (CNC) micromill: a computer aided design (CAD)

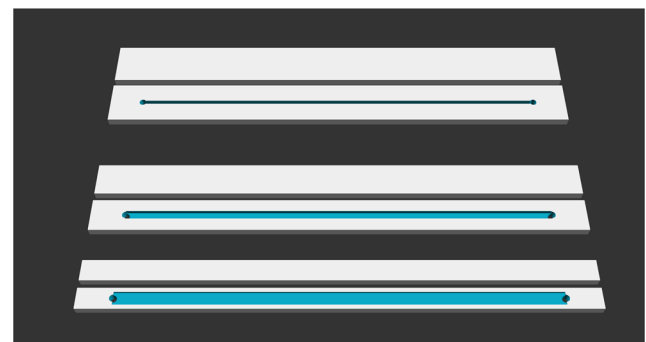


Fig. 3 Output solid geometry of Listing 2, which includes three different designs and their corresponding cover plates

tool is used to create a solid model of the device; computer aided manufacturing (CAM) software generates the commands (also called toolpaths) that are sent directly to the micromill; and control software manages the connection between a computer and the micromill and sends individual toolpaths to the micromill.

Device designs were created using OpenSCAD (Kintel and Wolf 2014), a free and open source CAD tool that reads script files to generate solid models. A custom library was used to create solid models using just the geometric parameters outlined in Fig. 2b as inputs. Figure 3 shows how an array of distinct solid models can be created from a few lines of code shown in Listing 2. This array of designs is spaced according to the size of the endmill used by the CNC to cut out each design, thus allowing for seamless processing by CAM software (Autodesk Fusion 360).

2.1.2 Fabrication

Micromilling has demonstrated advantages for low-volume prototyping of plastic microfluidic devices in terms of time and cost when compared to other fabrication methods such as embossing and injection molding (Guckenberger et al. 2015). While such studies claim that micromilling devices using an outside source can lower costs to \$137 per batch and 11–15 days of turn-around time, these costs only consider material costs and not labor, which can drive up the cost of prototyping an order of magnitude (Guckenberger et al. 2015). Costs per device can be lowered to less than \$1 if devices can be fabricated in-house; however, the costs associated with establishing such capabilities can be prohibitive. It is only very recently that high quality micromills have been available at low cost: as recently as 2015, micromills capable of achieving resolutions at or below $25\mu\text{m}$ were available for a minimum of \$15k (Guckenberger et al. 2015). The large footprints and noise associated with these machines made them inappropriate for use within a microfluidics laboratory. Additionally, the cost in terms of expertise required to operate a micromill is non-trivial. The software stack associated with generating toolpaths for a micromill does not currently resemble the simplicity of other CNC machines such as 3D printers. Traditional micromilling requires a suite of CAM tools that demand extensive knowledge of various tooling strategies such as feed rate, depth of cut and spindle speed that vary with each material and tool size.

Recent advances have led to a new class of desktop micromills, which can approach $25\mu\text{m}$ resolution at costs starting at \$2,500 all in a form-factor appropriate for a typical laboratory bench (Yen et al. 2016). While these new machines still require knowledge of CAD and CAM software tools, research in automation techniques specifically for micromilling microfluidics is beginning to bear

fruit (Silva et al. 2016; McDaniel et al. 2017). This study leverages these advancements to quickly manufacture distinct acoustofluidic device designs at a negligible cost when compared to outsourcing fabrication.

2.2 Device evaluation

We organized this study into four types of experiments: rapid screening, final screening, blood separation, and bacterial separation, progressing toward the selected design and then validating its performance in a series of functional tests. Rapid screening tests were conducted on two initial sets of designs for which the functionality of each design in the set could not be assumed, as shown in Fig. 1. The methodology for this test is outlined in Section 2.2.1. The results of these two initial rapid screening tests were then used to inform the parameter set of a final, more involved, screening test described in Section 2.2.2. Next, the winning geometry after final screening, hereafter referred to as

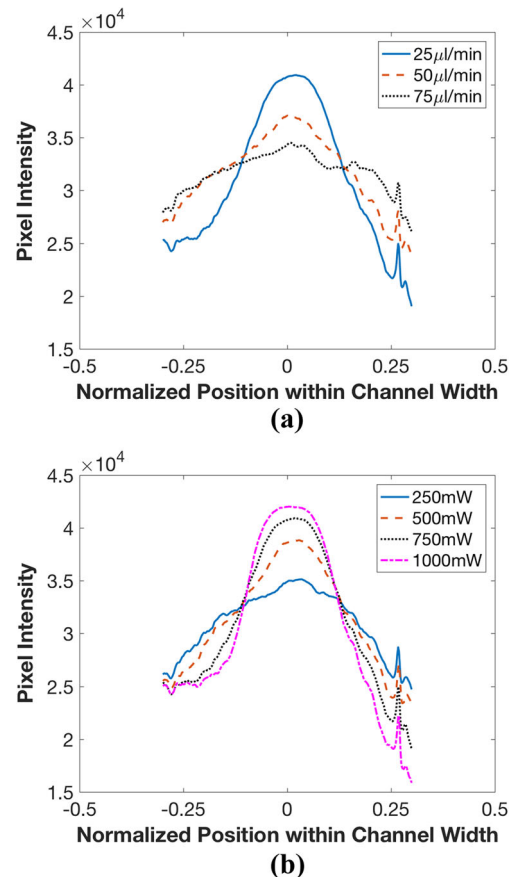


Fig. 4 Pixel intensity as a surrogate for RBC focusing performance. Inverted pixel grayscale values (i.e., darker areas have a higher value) across the width of the fluidic channel. **a** Power is held constant at 750 mW while flow rate is varied. Note that maximum pixel intensity, and thus focusing performance, increases as flow rate is decreased. **b** Flow rate is held constant at $25\mu\text{l}/\text{min}$, while power is varied. Note that focusing performance increases as power is increased

Chip 2.0, was compared to that of the baseline geometry in two different experiments measuring a device's ability to focus (i.e., concentrate in the center of the channel) RBCs. Finally, Chip 2.0 was compared to the baseline in experiments separating bacteria from diluted whole blood. The methodologies for each experiment are outlined in the subsections below.

The screening tests analyzed microscope images and derived pixel intensities as an indicator of RBC focusing performance. This method assumes that higher concentrations of RBCs will appear visibly darker, and hence have a higher inverse grayscale value, when better acoustic focusing is present (Barnkob et al. 2012). Figures 4 and 5, demonstrate that in conditions conducive to good focusing (ex., lower flow rate and higher dissipated power) the observable band of blood cells will appear narrower and darker and thus have a correspondingly higher inverse grayscale value within this band.

The two types of screening tests, rapid screening and final screening, each have different assumptions regarding the nature of their input parameter sets. In the rapid screening test a device may not exhibit acoustic focusing at any frequency under the experimental conditions; thus, the performance parameter determines the existence of acoustic focusing, but does not discern the relative quality of focusing between devices. In contrast, the final screening test attempts to compare the relative performance of devices that exhibit some acceptable measure of focusing.

The latter separation experiments measured a device's ability to maintain cell separation performance while minimizing dissipated power to the transducer (i.e. amplitude of acoustic excitation) and maximizing sample throughput (i.e., volumetric flow rate). Maximizing the volumetric flow rate will enable the largest volume of input sample to be enriched in the shortest amount of time. Minimizing the

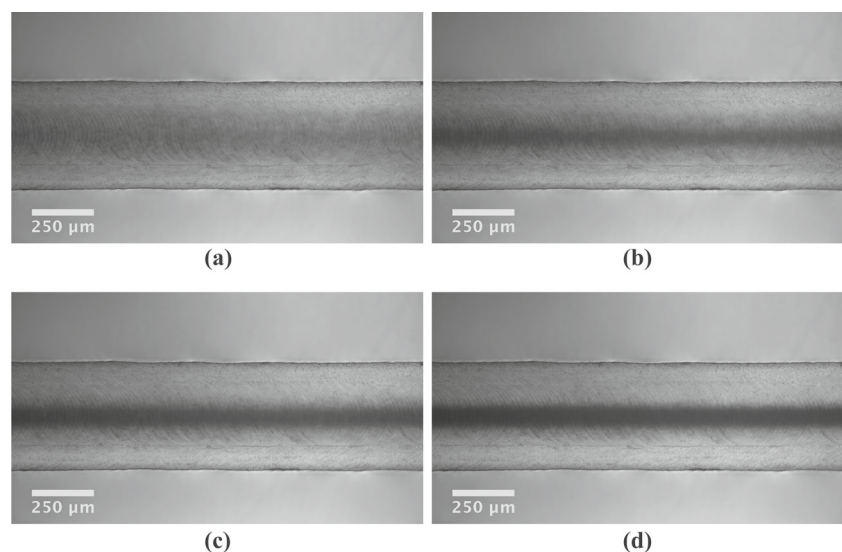
power requirements of the system is another important measure of merit because heat generated in the transducer and in the PS channel during actuation may lead to delamination of the channel or may be harmful to the clinical sample. Therefore, it is best to drive the system at the smallest amplitude necessary to achieve acceptable performance.

2.2.1 Rapid screening test

The purpose of the rapid screening test was to discover functional device designs, i.e., designs that could focus blood, and the frequencies at which they operate. Functionality of an acoustofluidic device was determined by analyzing the strength of focusing bands whose maxima occurs within the center fifth of the channel width, as the purpose of the device is to focus RBCs into the center channel of the trifurcation shown in Fig. 2. Thus, in order to affirm the decision node labeled "Focusing Observed Across Set" in Fig. 1, the point of maximum pixel intensity must be present in the center fifth of the channel for the device under test.

Each set of devices was tested under the same power and flow conditions while sweeping through a frequency band of 0.50 – 2.00 MHz. This range was informed by the optimum frequency of the baseline device (1.012 MHz). The transducer was selected with a resonant frequency of 2.34 MHz to avoid confounding effects of transducer resonance. The flow rate was set such that the average velocity in each chip was 1.94 cm/sec, a value that is equivalent to 100 μ l/min in the baseline device. The input power to the RF amplifier was set such that the average dissipated power at the transducer was 1 W at 1 MHz. Electrical equipment settings (ex., input voltage, RF amplifier gain, etc.) for this condition (i.e., 1 W at 1 MHz) were held constant as the frequency was varied. Within the tested bandwidth photos of the downstream end of the channel were taken in 10 kHz increments, from which

Fig. 5 Microscope images of focusing performance at resonant frequency with increasing power at levels of 250mW (a), 500mW (b), 750mW (c), 1000mW (d). The plots in Fig. 4b are derived directly from these images



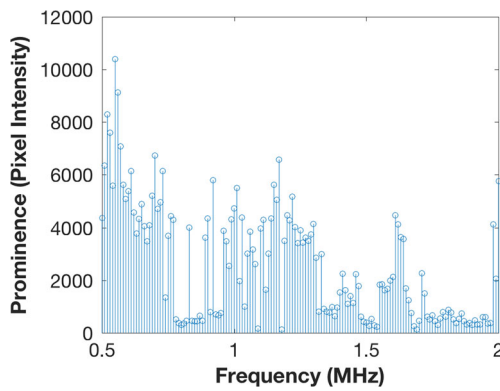


Fig. 6 Prominence versus Frequency for a fixed input voltage for device 4L9 in Table 1. Images were captured in 10 kHz increments over the bandwidth extending from 0.5 MHz to 2 MHz, inclusive

a number corresponding to the maximum peak prominence was returned. Prominence is a measure of a “peak” in pixel intensity and is defined further in the Methods section. The maximum peak prominence for the entire frequency sweep constituted the score for that particular design. An example frequency sweep is shown in Fig. 6.

2.2.2 Final screening test

The final screening test served to discriminate among devices that exhibited RBC focusing on the rapid screening test. This was accomplished by manually tuning the device to its optimum frequency (by visual inspection of the RBC focusing) and then modulating the measures of merit. Three flow rates (25 $\mu\text{l}/\text{min}$, 50 $\mu\text{l}/\text{min}$, and 75 $\mu\text{l}/\text{min}$) and four power levels (250 mW, 500 mW, 750 mW, and 1000 mW) were studied. A microscope image was captured for each combination of flow rate and power level, from which the ratio of peak prominence to width was calculated in

accordance with the method described in Section 3.2.2. The ratio of peak prominence to width serves as a predictor of the device’s ability to separate RBCs.

2.2.3 Blood separation test

The purpose of the blood separation test was to measure a device’s ability to focus RBCs to the center port of the device at a series of combinations of flow rate and power settings. A test of this sort has proven useful in assessing or comparing the acoustic energy density in several device configurations for applications ranging from high-throughput cell sorting (Adams et al. 2012; Mueller et al. 2013) to plasmapheresis (Lenshof et al. 2009). Samples of dilute whole blood were collected from both side and center ports for each setting according to the protocol established in Section 3.6. Performance was measured using RBC separation percentage, calculated by dividing the number of RBCs collected from the center port and dividing by the total number of RBCs collected from both outlet ports.

2.2.4 Bacterial separation test

The goal of the bacterial separation experiments was to determine the maximum capacity of a chip design in its ability to separate bacteria from blood, as has been demonstrated in other acoustic microfluidic devices (Ohlsson et al. 2016; Li et al. 2016). The operational capacity of a chip was evaluated in terms of the two measures of merit: volumetric flow rate and average dissipated power, each tested with the other fixed. Bacterial separation was measured at the point of minimum power or maximum flow rate required to achieve 90% separation of RBCs, measured by the ratio of colony forming units (CFU) to RBCs present in the side port. Where power was varied, flow rate was held at 50 $\mu\text{l}/\text{min}$. Where flow rate was varied, power was held at 1 W.

Table 1 Geometries tested for L9 design array with corresponding Chip ID

ID	W_c	H_c	W_s	Y_{Pos}	Prominence	f (MHz)
1L9	300	75	500	Low	6375	1.58
2L9	300	290	850	Center	5496	1.22
3L9	300	500	1200	High	8240	0.67
4L9	650	75	850	High	43021	0.55
5L9	650	290	1200	Low	12950	0.66
6L9	650	500	500	Center	13251	0.57
7L9	1000	75	1200	Center	14215	0.74
8L9	1000	290	500	High	9574	0.73
9L9	1000	500	850	Low	3144	0.71

All dimensions are given in units of μm . Prominence values are given in units of pixel intensity and correspond to each chip’s maximum prominence value for the tested bandwidth. The given frequencies indicate the point at which the maximum prominence was observed

3 Methods

3.1 Materials and assembly

Polystyrene (PS) was selected as an appropriate material based on its relatively low attenuation and high acoustic impedance relative to other plastics (Mueller et al. 2013; Selfridge 1985). The chip was sealed using a thermal bonding method previously described (Mueller et al. 2013). 20mm lengths of polyetheretherketone (PEEK) tubing served as an interface between the PS chip and the longer lengths of polyvinyl chloride (PVC) tubing used to introduce and collect sample. The rigid PEEK tubing was inserted into machined ports and affixed to the chip using epoxy (Epoxy 907, Miller-Stephenson, Danbury, CT, USA).

Lengths of vinyl capillary tubing were appended to the outlet ports to divide outlet volumes at a ratio of 60% volume measured at the side port to 40% at the center, using relative resistances.

The sealed chip was mounted to a lead zirconate titanate (PZT) transducer (APC International, PZT 850) with a nominal resonance of 2.34 MHz, using low viscosity cyanoacrylate adhesive.

3.2 Image processing and analysis

Image processing software (ImageJ Abràmoff et al. 2004) was used to measure pixel intensities across the width of the channel, W_c , from which prominence was calculated. The prominence of the focused stream, as described in detail in Section 3.2.1 below, served as a measure of the degree of focusing and the performance of the chip. Prominence has advantages over raw pixel intensity for the purposes of comparison due to its self-normalizing nature. Since prominence is measured relative to points on the signal itself it is robust against irregularities inherent to the signal. These irregularities can take the form of variable lighting conditions between experimental runs, such as variations in environmental lighting, and illumination variabilities within a single microscope image's region of interest, such as skewed background intensities caused by shadows.

3.2.1 Definition of prominence

Suppose an ordered signal is defined as in Eq. 1, where set D consists of N data points. Prominence is calculated by first finding all local maxima within the response set D and then determining a reference point on the signal associated with each local maxima (Freeman and Davis 1977; Arge et al. 2013). Briefly, this reference point is established by drawing a horizontal line in both the positive and negative directions from the local maxima (labeled as “Scan High” and “Scan Low”, respectively, in Fig. 7) until either the end

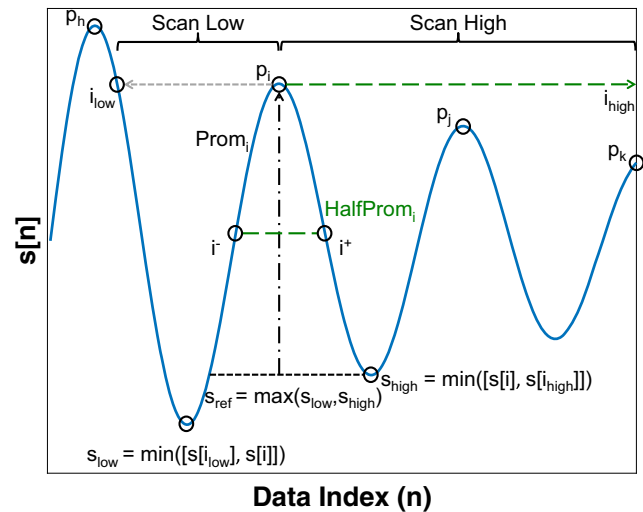


Fig. 7 Algorithmic progression. The blue, solid line represents a signal, $s[n]$, sampled at points, n , along the x-axis. Local maxima are labeled as points $p_{\{h,i,j,k\}}$. s_{ref} marks the reference point from which the prominence, $Prom_i$, of peak p_i is calculated. The width of the signal at the point of half-prominence, $HalfPromWidth$, is calculated by subtracting i^- from i^+

of the signal is reached (as in the case of i_{high} , in Fig. 7) or until the line intersects the signal itself (i_{low} , in Fig. 7), thus creating two sets of data points in the positive and negative directions. Minima are determined for each of the data sets, and prominence is then defined as the height of the local maxima relative to the maximum of these two established minima (s_{ref}).

$$s[n] = D \quad n = 0, 1, 2, \dots, N - 1 \quad (1)$$

A framework for defining prominence in more formal terms begins by establishing the data structure for the signal of interest. Individual values are accessed by index such that $s[i] = d_i, d_i \in D$. Two discrete points $d_i \in D$ and $d_{i'} \in D$ are said to be *neighbors* if $|i - i'| = 1$. A local maxima, hereafter called a *peak*, is a point p where d_i is greater than all of its neighbors, as defined in Algorithm 1 in Online Resource 1. The set of peaks $P \subset D$ consists of individual peak values $p \in P$. A peak is referenced by its index value i in D and the raw peak height is calculated by finding $s[i]$. The index in D of peak p is returned by the function $x(p)$. The height of peak p is returned by the function $s[x(p)]$. Thus if $p \leftarrow d_i, x(p) = i$ and $s[x(p)] = d_i$. Prominence is then determined via Algorithm 2 in Online Resource 1.

3.2.2 Definition of prominence to width ratio, χ

The half-prominence width of a peak of prominence $Prom$ is calculated by drawing two horizontal lines extending in the negative and positive directions from the point of half-prominence. These lines extend in either direction until

either the end of the signal is reached or the line intersects the signal itself. The indices of these events in the negative and positive directions are recorded as i^- and i^+ , respectively. The peak width *HalfPromWidth* is then defined as $|i^+ - i^-|$, as described in Algorithm 3 in Online Resource 1. We reason that for equivalent separation performance, assuming a fixed ratio of flow to side and center ports (Ley and Bruus 2016), that the prominence half width scales with the channel width, therefore it is appropriate to normalize the peak width by the width of the channel. The final equation for χ is shown in Eq. 2

$$\chi = Prom * \frac{W_c}{HalfPromWidth} \quad (2)$$

3.3 Transducer drive

The sinusoidal signal used to drive the transducer is generated by a function generator (AFG3022C, Tektronix, Beaverton, OR, USA) and amplified using a broadband RF amplifier (AG1021, T&C Power Conversion, Rochester, NY, USA). The instantaneous voltage and current across the transducer is monitored using an oscilloscope (DPO2024B, Tektronix, Beaverton, OR, USA). In order to determine the actual power consumed by the transducer, it is first necessary to consider the instantaneous power as follows:

$$P_{inst} = VI = V_{max}\sin(\omega t)I_{max}\sin(\omega t - \varphi), \quad (3)$$

where V_{max} and I_{max} are the maximum values of voltage and current, φ is the phase lag between the instantaneous current and voltage signals, and $\omega = 2\pi f$ is the sinusoidal drive frequency in rad/s. Using trigonometric identities and integrating over a cycle of the sinusoid we compute the average consumed power as:

$$P_{avg} = V_{rms}I_{rms}\cos\varphi, \quad (4)$$

where V_{rms} and I_{rms} are the root mean square values of voltage and current. Using the oscilloscope, we multiply the instantaneous voltage and current and compute the average of this product to find the average consumed power in real time throughout our experiments.

3.4 Blood sample preparation

All experiments in this study used de-identified fresh human whole blood purchased from a vendor (Research Blood Components, Brighton MA), anticoagulated with acid-citrate-dextrose. In each case, the blood was diluted to 5% by volume (for rapid screening tests) or 5% hematocrit (for all other tests) in phosphate buffer solution (PBS, 7.4 pH). Cellular concentrations were measured before and after dilution using an automated hematology analyzer (XP-300, Sysmex Co., Kobe, Japan). The diluted sample was then transferred to a 10 ml plastic syringe (BD 10 ml Luer-Lok

tip syringe 309604) and introduced to the chip through PVC tubing. The volumetric flow rate was regulated by a syringe pump (PhD Ultra, Harvard Apparatus).

3.5 Bacteria–blood sample preparation

Pseudomonas aeruginosa was incubated overnight in a Lysogeny Broth (LB) culture. It was diluted by a factor of 50 and incubated until it reached a mid log phase. A whole blood sample was diluted into PBS as described in Section 2.2.3. The optical density of the *Pseudomonas* culture was taken and the appropriate dilution was calculated to create solution consisting of whole blood diluted in PBS to 5% hematocrit and 10^5 *Pseudomonas* cells/ml.

3.6 Sample measurement

Blood or blood bacteria solutions were pumped through the device at its previously determined resonant frequency. For each device this was found visually by observing the focusing stream—the most compact stream reveals the resonant frequency. Outlet samples were collected in conical tubes after which they were measured and weighed for flow fraction and cell quantity calculations.

Blood content was measured via a hematology analyzer while bacterial content was measured through plating: the samples were weighed, then serially diluted in 10x steps into PBS. Each dilution was cultured onto a plate of LB agar and incubated at 37 °C overnight after which the CFU were counted.

The setpoint for 90% RBC separation for variable power and fixed flow (50 μ l/min) rate was accomplished by increasing power in small increments. Samples were collected from each output port and RBC counts were measured after each power increment. This process was repeated until a 90% RBC separation ratio was achieved between the side and center ports.

Determining 90% RBC separation for variable flow rate and fixed power (1 W) required that the flow rate be set to 25 μ l/min and increased in increments until such a point as 90% RBC separation was achieved.

4 Results

4.1 Screening design of experiments

Experiments must be initialized such that the sampling of the solution space can detect curvature in the response, as described in Section 4.2. Curvature in the response surface for an explanatory variable implies the existence of a local maxima in performance. Driving the design towards that local maxima is accomplished by isolating the variable in

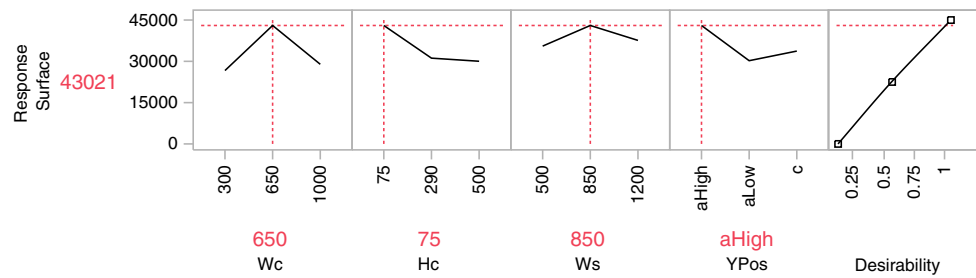


Fig. 8 Results of design space seeding. The quantities on the vertical axis correspond to the prominence data shown in Table 1. The response surface is determined through a least squares fit of the aforementioned

prominence values in four-dimensional space. The red dashed lines demarcate the points of maximum desirability

question and conducting experiments at adjacent points on the response plane, as outlined in Section 4.3.

Figure 2 illustrates the explanatory variables studied. Channel Width (W_c), channel height (H_c), side-wall width (W_s) and the position of the channel on the y -axis in two dimensional space (Y_{pos}) were selected as variables to study because they account for a majority of the two-dimensional design-space and are simple to vary during fabrication.

4.2 Seeding of the design space (rapid screening test)

In order to economize the number of rapid screening experimental runs, an orthogonal array was chosen to generate a useful parameter set for the initial experiments. Orthogonal arrays are used in design optimization to provide the most coverage of the solution space while minimizing the number of experimental runs (Yokoyama and et al. 1993). This is accomplished through the creation of an experimental set such that each combination of the array's strength appears equally often (Hedayat et al. 2012). The orthogonal array used to seed the design space is known as the $L_9(3^4)$ array, which has a strength of two and is used to probe a solution space consisting of four explanatory variables at three settings in nine experimental runs, as opposed to the 81 experimental runs required to conduct the full-factorial experiment (Hedayat et al. 2012). The use of three explanatory variable settings was chosen in order to

detect curvature in the response surface. The parameter set tested while seeding the design space, in accordance with an $L_9(3^4)$ orthogonal array, is shown in Table 1.

The response surface generated from the data points shown in Table 1 was analyzed using statistical software (JMP, Version 13.0.0. SAS Institute Inc., Cary, NC, 1989-2017) and is shown in Fig. 8. Maximum desirability of the performance parameter (prominence) was achieved by chip 4L9, which had W_c set to $650\mu\text{m}$, H_c to $75\mu\text{m}$, W_s to $850\mu\text{m}$ and placing the channel in the high vertical position. Additionally, the response surface shows significant curvature while modulating the width of the channel, leading into the next iteration of the study outlined in Section 4.3.1.

4.3 Variable isolation studies

4.3.1 Channel width study (rapid screening test)

Proceeding from the results of the initial seeding of the design space, we fixed the other parameters from the best geometry (4L9) and varied the channel width in $50\mu\text{m}$ increments. Although the response surface indicates that thinner channel height may be preferable, we selected a height of $100\mu\text{m}$ for this variable isolation study, anticipating that a slightly greater channel height would have practical advantages.

Table 2 Geometries tested for an isolation study of channel width with corresponding Chip ID

ID	W_c	H_c	W_s	Y_{Pos}	Prominence	f (MHz)
1Wc	500	100	850	High	12143	0.64
2Wc	550	100	850	High	15200	0.51
3Wc	600	100	850	High	4770	1.58
4Wc	650	100	850	High	5470	1.99
5Wc	700	100	850	High	-	-

All dimensions are given in units of μm . Prominence values are given in units of pixel intensity and correspond to each chip's maximum prominence value for the tested bandwidth. The given frequencies indicate the point at which the maximum prominence was observed. The frequency range scanned spanned from 500 kHz to 2 MHz. No focusing was observed within this range for the design with a channel width of $700\mu\text{m}$

Table 3 Geometries tested for a final screening study of channel height with corresponding Chip ID

ID	W_c	H_c	W_s	Y_{Pos}	f (MHz)
1Hc	550	100	850	High	0.684
2Hc	550	150	850	High	0.640
3Hc	550	200	850	High	0.634
4Hc	550	250	850	High	0.632
5Hc	550	300	850	High	0.640

All dimensions are given in units of μm . The listed frequencies coincide with the locations of the corresponding device's fundamental odd resonant mode

As shown in Table 2, the highest performing channel width, holding other factors constant, was $550\mu\text{m}$. Channels having a width of $600\mu\text{m}$ and above demonstrated the ability to focus RBCs to the center fifth of the channel, however the focusing was a result of driving the chip at a higher order mode thus creating more than one focusing band across the channel width.

As a significant performance shift was observed as a result of a small adjustment to H_c , channel height was chosen as the variable to isolate for the next design set.

4.3.2 Channel height study (final screening test)

This design set fixed values for W_c , W_s , and Y_{Pos} while varying H_c resulting in the geometries shown in Table 3. All devices in this set demonstrated focusing of blood; the frequencies for which are shown in Table 3. This study was conducted in accordance with the final screening test specified in Section 2.2.2. The results shown in Fig. 9 demonstrate that, for flow rates higher than $25\mu\text{l/min}$, the chip with a channel height of $250\mu\text{m}$ performed better than the other chips tested in terms of χ at all studied power levels. Thus the winning geometry of the study's device screening stage has a channel width of $550\mu\text{m}$, a channel

height of $250\mu\text{m}$, a side-wall width of $850\mu\text{m}$, with the channel in the high vertical position (i.e., Chip 4Hc in Table 3).

4.4 Comparison of chip 2.0 versus baseline geometry

The results of the screening tests shown in Fig. 9 yield a geometry that outperformed the other devices in terms of RBC focusing analyzed by image analysis. However, in order to gauge the ultimate success of this geometry it was tested against the baseline geometry. This section presents results from three experiments that compared the winning geometry of the screening tests (i.e., Chip 2.0) against the baseline geometry through image analysis, blood separation, and bacteria separation.

4.4.1 Comparative focusing

Figure 10a–c plots the performance of Chip 2.0 against the baseline in terms of χ . The results show that Chip 2.0 outperforms the baseline for all tested combinations of flow and power settings.

Voltages and currents used to achieve 1 W of dissipated power at resonant frequencies for the baseline geometry and Chip 2.0 are shown in Table 4. Note that the drive is

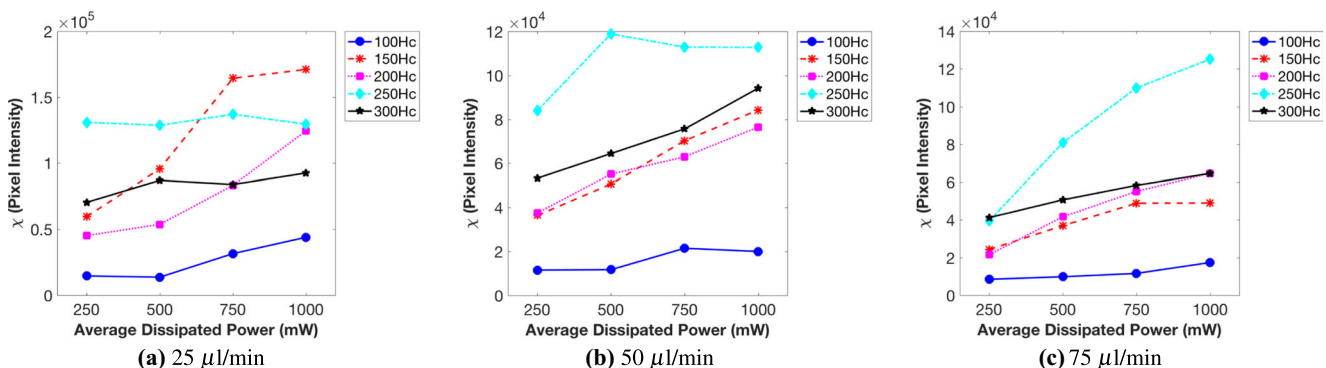


Fig. 9 Performance comparison of channel height study using image analysis. **a–c** plot the performance of the geometries in Table 3 for three volumetric flow rates: $25\mu\text{l/min}$, $50\mu\text{l/min}$ and $75\mu\text{l/min}$,

respectively. Performance was calculated from microscope images in the manner described in Section 3.2.2. Datasets are shown for each channel height from 100 to $300\mu\text{m}$

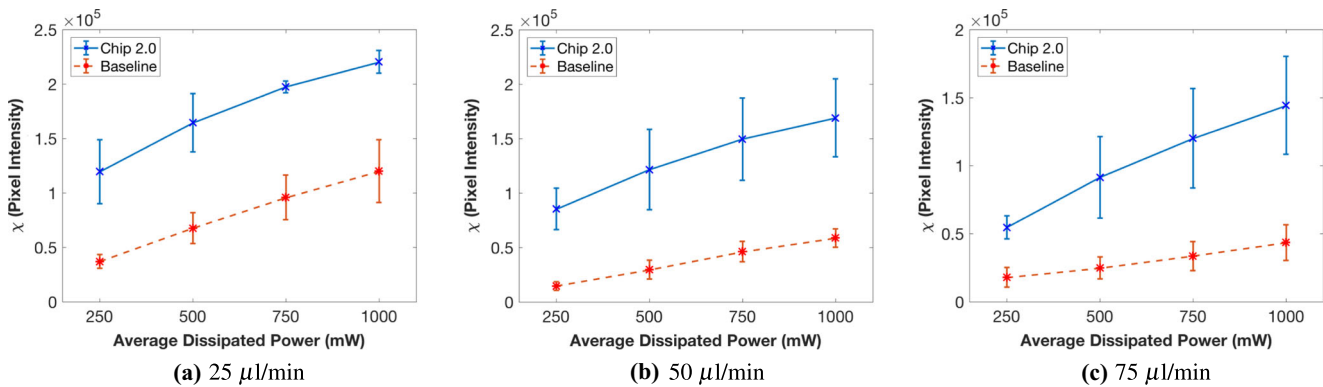


Fig. 10 Performance comparison versus baseline using image analysis. **a–c** plot the performance of the baseline versus the winner of the study for three volumetric flow rates: 25 $\mu\text{l}/\text{min}$, 50 $\mu\text{l}/\text{min}$ and

75 $\mu\text{l}/\text{min}$, respectively. Performance was calculated from microscope images in the manner described in Section 3.2.2

not optimized for impedance matching to the transducer, therefore most power is reflected.

4.4.2 Comparative blood separation

Figure 11 plots the performance of Chip 2.0 against the baseline in terms of each device's ability to focus RBCs to the center port as measured by cell counts in the outlet fractions. The dynamic range of each measurement was limited between the control measurement (i.e., zero average dissipated power) and 100% RBC concentration in the center channel. As the chip has two outlet ports (Fig. 2), RBCs will be approximately equally distributed between them in the acoustics-off (0 W input power) condition. The baseline and Chip 2.0 demonstrated comparable performance at a flow rate of 25 $\mu\text{l}/\text{min}$ across all power settings; however, at higher flow rates Chip 2.0 outperformed the baseline across all non-control power settings.

4.4.3 Comparative bacterial separation

Four experiments were conducted in three technical replicates, two for each device design (baseline and Chip 2.0), in order to determine the optimal value for each measure of merit while holding the other constant. Optimality was defined as the maximum flow rate or minimum power required to maintain at least 90% RBC separation between

the side and center ports while bacteria recovery in the side port was measured.

The results in Fig. 12 show that Chip 2.0 achieved a 175% increase in throughput relative to the baseline. Additionally, Chip 2.0 was able to decrease the average dissipated power by 81.63% when compared to that of the baseline geometry. The actual average RBC separation across all four experiments was 95.25% ($\pm 1.89\%$). The yield of the bacterial samples collected at the side port had a standard deviation of 0.05%. For both devices the yield of bacteria in the side port was 33.5% ($\pm 3\%$) after separation, showing that separation performance in the 2.0 design is equal to that of the baseline while enabling lower driving power and/or higher throughput.

It is worth noting that the Chip 2.0 design achieved better RBC separation for both the maximum flow rate and minimum power experiments (98% vs 94% and 95% vs 94%, respectively) and equivalent bacterial recovery relative to the baseline across all four experiments; thus, for each Chip 2.0 experiment the measure of merit (flow or power) could show greater advantages if the RBC yield were adjusted to match that of the baseline.

5 Discussion

The resonant response of acoustophoretic microfluidic devices has been shown to be non-linear (Garofalo et al. 2016;

Table 4 Baseline versus Chip 2.0. All dimensions are given in units of μm

Chip	W_c	H_c	W_s	Y_{Pos}	f (MHz)	Voltage @ 1 W (V_{pp})	Current @ 1 W (mA_{pp})
Chip 2.0	550	250	850	High	0.632	56.44 (± 2.4)	1039 (± 53)
Baseline	430	200	1055	High	1.012	45.78 (± 1.86)	1340 (± 70)

Standard operating conditions, measured at the transducer, are provided for frequencies, input voltages and currents required to achieve 1 W of average dissipated power. These conditions are the values for which the fundamental resonant odd modes for each chip were achieved

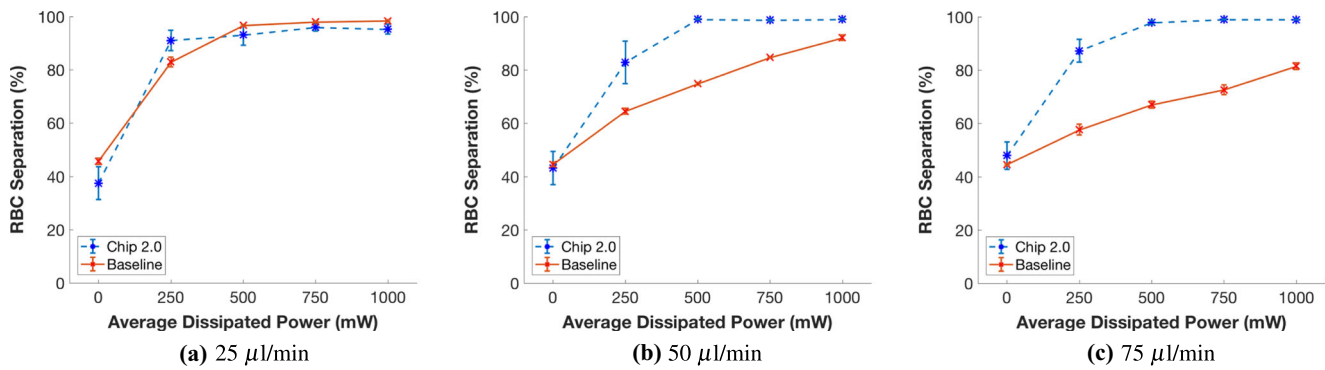


Fig. 11 Blood separation performance comparison versus baseline. **a–c** plot the performance of the baseline versus the winner of the study for three volumetric flow rates: 25 $\mu\text{l/min}$, 50 $\mu\text{l/min}$ and 75 $\mu\text{l/min}$, respectively. Performance is defined based on each design's ability to

focus RBCs into the middle channel of the trifurcation shown in Fig. 2. RBC separation is defined as the number of RBCs measured at the center port divided by the total number of RBCs measured at the input port

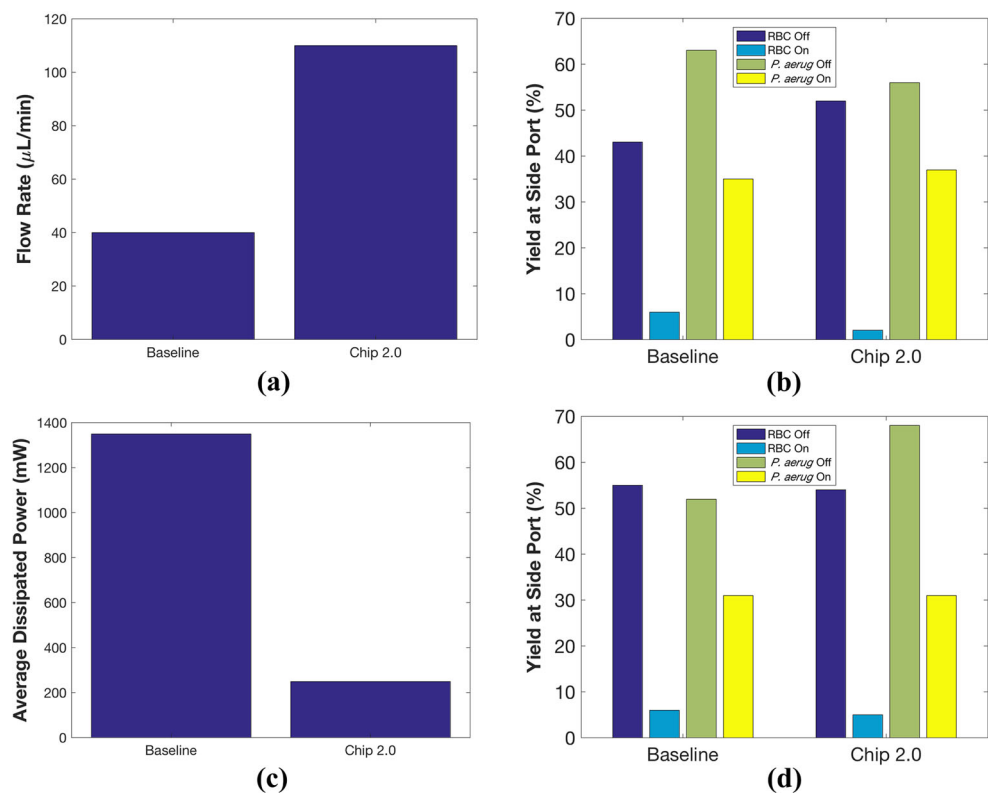
Bora and Shusteff 2015; Glynn-Jones et al. 2009; Hahn et al. 2014). Complex response patterns with numerous explanatory variables have been successfully optimized using a fractional factorial experimental design approach in conjunction with a response surface methodology (Khuri and Mukhopadhyay 2010); however, these methodologies assume that the function $f(x)$ modeling the response variable y to the explanatory variables $x = (x_1, x_2, \dots, x_n)$ accounting for some experimental error ϵ , as shown in

Eq. 5, is a low-degree polynomial (Khuri and Mukhopadhyay 2010),

$$y = f(x) + \epsilon \quad (5)$$

In the absence of a near-quadratic response, multiple rounds of experiments are required to adequately detect a positive gradient in performance (Carley et al. 2004). Even after multiple rounds of experiments, the nature of a complex response surface means that no claim of optimality can

Fig. 12 Levels of each measure of merit required to achieve equivalent separation performance. **a** shows the relative performance of the baseline as it compares to Chip 2.0 in terms of flow rate with power held constant at 1 W. **(b)** illustrates the actual performance of each chip at the levels specified in **(a)** in both the acoustics “off” (0 W and established chip flow rate) and “on” (1 W and established chip flow rate) conditions. **c** summarizes the performance of the two chip designs holding flow rate at 50 $\mu\text{l/min}$ while varying power. Constant values were maintained for RBC separation and bacterial recovery for all chip designs and experiments. **d** depicts the performance of each device at the power levels specified in **(c)**; “off” being the control condition of 0 W and 50 $\mu\text{l/min}$



be made (Box 2006). Since this study seeks a performance enhancement, as opposed to a rigorous optimal geometry, this iterative method is acceptable.

This study successfully improved the performance of the acoustic separator chip for both measures of merit. However, Chip 2.0 may not represent an optimal design, and further improvement is likely possible. The experimental design selected parameters that were most accessible to systematic variation. For example, the impact of total height of the device was not explored because changes in sheet stock thickness would require sourcing or custom fabricating those sheets, and the bond process would have to be adjusted for each thickness. Likewise, the selection of the values tested assumes a more or less smoothly varying response. Further analysis is needed to rigorously support that assumption.

The frequency range studied for the rapid screening tests (0.5 – 2.0 MHz) was chosen based on the known resonance of the baseline device (approximately 1 MHz) and the expectation that small variations in dimensions should result in comparably small variations in resonant frequency. Additionally, the lower limit was selected with the knowledge that acoustic radiation force scales with frequency and lower frequencies could limit the ability of the device to focus small cells or particles such as platelets or bacteria, if desired in other applications. Furthermore, there were practical experimental limitations at the upper end of the range; a transducer with a higher resonant frequency (ex., 5 MHz) would allow a wider range of frequencies to be explored, however the fragility of such transducers increases the difficulty of mounting and testing the devices. Nevertheless reproducing the screening with a wider frequency range, particularly at the low end could yield further improvements.

Despite these and other limitations, this study was meant not only to identify an improved geometry, but also to establish a method for empirical development of devices. The resulting performance improvement, as measured by the bacteria separation task, suggest that the initial screening using only image-based analysis of RBC focusing provides a useful approach for assessing devices. To perform the setup, operation, output sample collection, and cell counting in the final bacteria separation takes several hours at least with all parameters fixed, whereas hundreds of image-based prominence measurements could be made at a rate of one every 15 seconds, while sweeping frequency.

Future explorations of device designs can be enabled by this parametric, rapid prototyping framework, which is part of a larger workflow (Lashkaripour et al. 2017; Lippai et al. 2017; Sanka et al. 2017). The 19 devices designed in this manuscript can take advantage of this process with a high level description of the device functionality, microfluidic primitives, and automated fabrication and control.

6 Conclusion

Enabled by a parametric, rapid prototyping framework, we were able to screen 19 device designs, distinct in four geometric parameters, towards optimizing the performance of a blood–bacteria separation device. Compared to the previously published plastic design, we demonstrate that the improved device geometry can separate blood and bacteria while operating at 175% greater flow rate as well as reducing the power requirement by 81.63% for equivalent separation performance. The improved device will offer increased throughput and reduced power requirements and could aid performance of plastic acoustofluidic devices for future point-of-care assays.

Acknowledgments This research was made possible by the Draper Laboratory Fellowship program in conjunction with the US Air Force Academy Faculty Pipeline Fellowship. Douglas Densmore was funded in part by NSF Award #1522074.

References

- M.D. Abràmoff, P.J. Magalhães, S.J. Ram, Image processing with imagej. *Biophoton. Int.* **11**(7), 36–43 (2004)
- J.D. Adams, C.L. Ebbesen, R. Barnkob, A.H. Yang, H.T. Soh, H. Bruus, High-throughput, temperature-controlled microchannel acoustophoresis device made with rapid prototyping. *J. Micromech. Microeng.* **22**(7), 075017 (2012)
- M. Antfolk, T. Laurell, Continuous flow microfluidic separation and processing of rare cells and bioparticles found in blood—a review. *Analytica Chimica Acta* (2017)
- L. Arge, M. De Berg, C. Tsirogiannis, Algorithms for computing prominence on grid terrains. in *Proceedings of the 21st ACM SIGSPATIAL International Conference on Advances in Geographic Information Systems* (ACM, 2013), pp. 254–263
- R. Barnkob, H. Bruus, Acoustofluidics: theory and simulation of radiation forces at ultrasound resonances in microfluidic devices. in *Proceedings of Meetings on Acoustics 157ASA*, Vol. 6 (ASA, 2009), p. 020001
- R. Barnkob, I. Iranmanesh, M. Wiklund, H. Bruus, Measuring acoustic energy density in microchannel acoustophoresis using a simple and rapid light-intensity method. *Lab Chip* **12**(13), 2337–2344 (2012)
- A.A.S. Bhagat, H. Bow, H.W. Hou, S.J. Tan, J. Han, C.T. Lim, Microfluidics for cell separation. *Med. Biol. Eng. Comput.* **48**(10), 999–1014 (2010)
- M. Bora, M. Shusteff, Efficient coupling of acoustic modes in microfluidic channel devices. *Lab Chip* **15**(15), 3192–3202 (2015)
- G.E. Box, Improving almost anything: Ideas and essays, vol. 629. Wiley-Interscience (2006)
- H. Bruus, Acoustofluidics 2: Perturbation theory and ultrasound resonance modes. *Lab Chip* **12**(1), 20–28 (2012)
- K.M. Carley, N.Y. Kamneva, J. Reminga, Response surface methodology. Technical report, DTIC Document (2004)
- H. Freeman, L.S. Davis, A corner-finding algorithm for chain-coded curves. *IEEE Trans. Comput.* **26**(3), 297–303 (1977)
- F. Garofalo, T. Laurell, H. Bruus, Performance study of acoustophoretic microfluidic silicon-glass devices by characterization of material and geometry dependent frequency spectra. *arXiv:1610.02794* (2016)

- P. Glynne-Jones, R.J. Boltryk, M. Hill, N.R. Harris, A new thin-reflector mode for ultrasonic particle manipulation in layered resonators. in *2009 IEEE International Ultrasonics Symposium (IUS)* (IEEE, 2009), pp. 2137–2140
- D.J. Guckenberger, T.E. De Groot, A.M. Wan, D.J. Beebe, E.W. Young, Micromilling: a method for ultra-rapid prototyping of plastic microfluidic devices. *Lab Chip* **15**(11), 2364–2378 (2015)
- P. Hahn, O. Schwab, J. Dual, Modeling and optimization of acoustofluidic micro-devices. *Lab Chip* **14**(20), 3937–3948 (2014)
- M. Hecke, W. Schomburg, Review on micro molding of thermoplastic polymers. *J. Micromech. Microeng.* **14**(3), R1 (2003)
- A.S. Hedayat, N.J.A. Sloane, J. Stufken, Orthogonal arrays: theory and applications. Springer Science & Business Media (2012)
- M. Hill, R.J. Townsend, N.R. Harris, Modelling for the robust design of layered resonators for ultrasonic particle manipulation. *Ultrasonics* **48**(6), 521–528 (2008)
- A.I. Khuri, S. Mukhopadhyay, Response surface methodology. Wiley Interdiscip. Rev. Comput. Stat. **2**(2), 128–149 (2010)
- M. Kintel, C. Wolf, Openscad. GNU General Public License, p GNU General Public License (2014)
- A. Lashkaripour, R. Sanka, J. Lippai, D. Densmore, Design automation based on fluid dynamics. in *The Proceedings of the 9th International Workshop on Bio-Design Automation*, (2017)
- A. Lenshof, A. Ahmad-Tajudin, K. Jarås, A.-M. Sward-Nilsson, L. Åberg, G. Marko-Varga, J. Malm, H. Lilja, T. Laurell, Acoustic whole blood plasmapheresis chip for prostate specific antigen microarray diagnostics. *Anal. Chem.* **81**(15), 6030–6037 (2009)
- M.W. Ley, H. Bruus, Continuum modeling of hydrodynamic particle–particle interactions in microfluidic high-concentration suspensions. *Lab Chip* **16**(7), 1178–1188 (2016)
- S. Li, F. Ma, H. Bachman, C.E. Cameron, X. Zeng, T.J. Huang, Acoustofluidic bacteria separation. *J. Micromech. Microeng.* **27**(1), 015031 (2016)
- J. Lippai, R. Sanka, A. Lashkaripour, D. Densmore, Function-driven, graphical design tool for microfluidic chips: 3duf. in *The Proceedings of the 9th International Workshop on Bio-Design Automation*, (2017)
- J. McDaniel, W.H. Grover, P. Brisk, The case for semi-automated design of microfluidic very large scale integration (mvlsi) chips. in *2017 Design, Automation & Test in Europe Conference & Exhibition (DATE)* (IEEE, 2017), pp. 1793–1798
- A. Mueller, A. Lever, T. Nguyen, J. Comolli, J. Fiering, Continuous acoustic separation in a thermoplastic microchannel. *J. Micromech. Microeng.* **23**(12), 125006 (2013)
- P.N. Nge, C.I. Rogers, A.T. Woolley, Advances in microfluidic materials, functions, integration, and applications. *Chem. Rev.* **113**(4), 2550–2583 (2013)
- P. Ohlsson, M. Evander, K. Petersson, L. Mellhammar, A. Lehmusvuori, U. Karhunen, M. Soikkeli, T. Seppä, E. Tuunainen, A. Spangar, et al., Integrated acoustic separation, enrichment, and microchip polymerase chain reaction detection of bacteria from blood for rapid sepsis diagnostics. *Anal. Chem.* **88**(19), 9403–9411 (2016)
- R. Sanka, J. Lippai, D. Densmore, mlsi design with mint. in *The Proceedings of the 9th International Workshop on Bio-Design Automation*, (2017)
- A.R. Selfridge, Approximate material properties in isotropic materials. *IEEE Trans. Sonics Ultrason.* **32**(3), 381–394 (1985)
- M. Settles, H. Bruus, Forces acting on a small particle in an acoustical field in a viscous fluid. *Phys. Rev. E* **85**(1), 016327 (2012)
- R. Silva, R. Sanka, D. Densmore, Makerfluidics: Microfluidics for the masses. in *The Proceedings of the 8th International Workshop on Bio-Design Automation*, (2016), pp. 63–64
- D.P. Yen, Y. Ando, K. Shen, A cost-effective micromilling platform for rapid prototyping of microdevices. *Technology* **4**(04), 234–239 (2016)
- Y. Yokoyama, et al., Taguchi methods: design of experiments, volume 4. Amer Supplier Institute (1993)